Journal Pre-proof

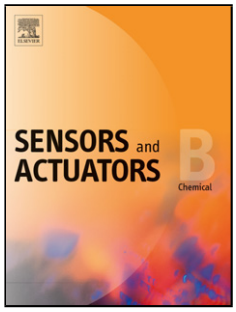

WO_3 processed by direct laser interference patterning for NO_2 detection

L. Parellada-Monreal, S. Gherardi, G. Zonta, C. Malagù, D. Casotti, G. Cruciani, V. Guidi, M. Martínez-Calderón, I. Castro-Hurtado, D. Gamarra, J. Lozano, L. Presmanes, G.G. Mandayo

PII: S0925-4005(19)31425-X

DOI: https://doi.org/10.1016/j.snb.2019.127226

Reference: SNB 127226

To appear in: *Sensors and Actuators: B. Chemical*

Received Date: 11 February 2019

Revised Date: 11 September 2019

Accepted Date: 2 October 2019

Please cite this article as: { doi: https://doi.org/

Acknowledgement

This work was supported by the Ministry of Economy and Competitiveness (MINECO) through the TEMIN-AIR+ (project n°. TEC2016-79898-C6-3-R) and by the Basque Government under the Elkartek program (MICRO4FAB grant n°. KK-2016-00030). All the authors thank the technical and human support provided by Facility of Analysis and Characterization of Solids and Surfaces of SAIUEx-UEx for the TOF-SIMS and SEM measurements. The authors also wish to thank SCENT s. r. l. for financing this research.

Authors' biographies

Laura Parellada Monreal received her BS degree in Physics from the University of Barcelona in 2013 and her MSc degree in Nanophysics and Nanostructures from the University Joseph Fourier in Grenoble (France) in 2015. Since 2016, she is a PhD student in the Micro and Nano Systems Research Line. Her PhD project is focused on semiconductor materials nanostructured by laser techniques for gas sensing on environmental applications.

Sandro Gherardi received his Bachelor's Degree in Tecnologie Fisiche Innovative (TFI) in 2002, with a thesis addressed to the study of the electrical response to various pollutant gases, based on nanostructured gas sensors and performed at the Sensors and Semiconductors Laboratory of the Department of Physics and Earth Sciences of University of Ferrara, where is today employed as assistant engineer. He continues to deal with environmental/industrial sensors, conducting researches on semiconductor materials for solid state sensors, installation of environmental monitoring and industrial control units, optimization and implementation of compressed gas transmission lines, in various programming languages and communication interfaces with laboratory equipment. From September 2016 is employed as IT manager at SCENT S.r.l.

Giulia Zonta received the Bachelor's Degree in Physics and Astrophysics in December 2010 (110/110 cum laude) and the Master's Degree in Physics in October 2013 (110/110), at the University of Ferrara. In April 2017, she received her Ph.D. in Matter Physics, working with the Sensors Team, coordinated by Prof. Cesare Malagù. Currently her post-doc research focuses on the study of the physico-chemical behaviour of chemoresistive nanostructured gas sensors put in contact with volatile organic compounds (VOCs) of medical interest. She is the Sales Executive and co-founder of the start-up SCENT S.r.l, with the aim to create prototypes for tumour preventive screening and monitoring and with SCENT team, she won diverse competitions as Premio Marzotto 2015.

Cesare Malagù was born in 1974 in Ferrara, Italy. He received a degree in Physics at the University of Ferrara in 1997 (Summa Cum Laude) and the Ph.D. in experimental physics in 2001. He has been teaching General Physics since 2001 and has been a Lecturer since 2007. His research activity is based on modelling of transport phenomena in nanostructured semiconductors. His expertise regards thick-film gas sensors applied to environmental monitoring and cancer screening. He has 75 papers in peer-reviewed journals (Hirsch index 29) and numerous proceedings and invited lectures; moreover, he is in the editorial board of several journals. He has been coordinating the sensors group at the University of Ferrara since 2010 and he is an associate professor since 2016.

Davide Casotti: Bachelor in Geology at the University of Ferrara in 2010. He got his Ph.D. In 2017 in Physic and Nanosciences at University of Modena and Reggio Emilia. Research activity has focused on nanomaterials (powders and thin films), gas sensors, and monocrystals characterization.

Giuseppe Cruciani is Full Professor of Mineralogy at the Department of Physics and Earth Sciences, University of Ferrara. Graduate with honour in Geological Sciences in 1989 at the University of Perugia where he got a PhD in Mineralogy (Crystallography) and Petrology in 1993. Visiting scientist in 1995 at the European Synchrotron Radiation

Facility (ESRF) in Grenoble, France, there he served in the chemistry review committee for project selection from 2008 to 2010. Since 2016 is Chair of proposal review panel for hard condensed matter-structures at the Elettra synchrotron in Trieste, Italy. Past President 2012-2013 of the Italian Society of Mineralogy and Petrology, is currently (2016-2019) President of the Italian Zeolite Association. Serves as Associate Editor of the European Journal of Mineralogy. Major research fields in crystallography and crystal-chemistry of microporous materials and oxide systems for wide application fields. Experimental skills mostly focused on single crystal and powder diffraction, both with conventional X-rays and large scale facility radiation (synchrotron X-rays and neutrons). Author of about 150 articles in international journals and more than 10 book chapters, with 2795 citations, his H-index is equal to 30 (January 2019).

Vincenzo Guidi: Co-founder in 1996 of the Sensors and Semiconductors Lab (SSL) at Ferrara University with the aim to study nano-phased metal oxides for gas sensing via chemo-resistive effect. In particular, he studied the correlation existing between gas-sensitivity of films vs. structural features of the sensing materials. It was pursued the investigation of novel materials for gas sensing and some methods for their deposition were established. Information on basic sensing mechanisms and on grain coalescence in metal-oxides were found out as well as new methods for grain-growth inhibition. He deepened the understanding of gas sensing also from the theoretical standpoint. Some models highlighting the effects of small dimensionality of nanograins and their correlation to the gas-sensing qualities were put forward. He has been organiser of national and international projects and events on chemical sensors and actively played editorial roles. Professor since 2006, he is currently Director of the Department of Physics and Earth Sciences of Ferrara University.

Miguel Martínez Calderón received his bachelor degree in Materials Engineering from Polytechnique University of Madrid in 2013. He also obtained a Master's degree in Biomedical Engineering from the same university in 2014. In May 2018, he received his Ph.D in applied engineering working with the Additive Manufacturing and Laser group of CEIT, in the Materials & Manufacturing division. Currently he works at the same institution as a junior researcher and his work is focused on the development of advanced functional surfaces based on ultrafast laser technology and its application. His research interest includes ultrafast processes in materials, micro and nano structuring of materials surfaces, development of advanced surfaces applications and phenomena related to the interaction of light with matter in the micro/nano scale.

Irene Castro Hurtado received her BS degree in Physics from the University of the Basque Country in 2008 and her PhD degree in Physics from the University of Navarra, San Sebastián, in 2011. In 2008, she joined Ceit-IK4 as a researcher of the Sensors & Analog Electronics Group, focusing her work on industrial monitoring applications. Her main research interests are in the field of materials science, solid state physics and micro and nanotechnology. She joined CIC Energigune in 2017 as a postdoc for developing solid state batteries for industrial projects. Since 2018, she works at Tubacex as metallurgy responsible for the Quality department. She is author or co-author of more than 15 scientific papers in peer-reviewed international journals and more than 20 presentations at international conferences. She has been lecturer of Materials Science and Fabrication of Electronics Systems at Tecnun, Engineering School of the University of Navarra from 2008 to 2017.

Daniel Gamarra received the Degree in Chemistry in 2003 from University of Granada, Spain and Ph.D. degree in 2008 from Universidad Autonoma de Madrid, Spain. He has worked in Nanostructured Catalysts for Energy department of Instituto de Catalisis y Petroleoquimica (CSIC) in new catalytic systems based in copper and cerium mixed for CO preferential oxidation in hydrogen rich current (application in PEM fuel cells) and for anode systems in SOFC fuel cells. His Post Ph.D. working was carried out in the same place about new catalytic supports of Cerium oxide with exposure of thermodynamically unstable faces for preferential CO oxidation and hydrothermal synthesis method of new materials sulphured for solar cells applications. His actual career is associated to Manager Technician in solid and surface characterization analytic service in University of Extremadura and "ICTs NANBIOSIS" (Spanish singular scientific technical installation). His research interests include new advances in surface characterization by TOF-SIMS, XPS and other technics.

Jesús Lozano received the B. Sc. degree in Electronic Engineer in 2001 and Ph. D. degree in 2005 from Universidad Complutense de Madrid, Spain. He has worked in instrumentation systems at Electronics Department of the University Complutense of Madrid, in chemical sensors and electronic noses at the Laboratorio de Sensores, Consejo Superior de Investigaciones Científicas (CSIC), Madrid, in control, modelling and simulation at Naval Engineering School of Universidad Politécnica de Madrid. Presently, he works as associate professor at the Industrial Engineering School of Universidad de Extremadura, Badajoz. His research interests include gas sensors, instrumentation and measurement systems, and pattern recognition techniques.

Lionel Presmanes received his PhD degree, for his thesis-work on ferrite thin films for magneto-optical storage. Since 1997, he has been working in CIRIMAT laboratory at University Paul Sabatier (Toulouse) and he is also CNRS researcher since 2001. His research interests are focused on the preparation of sputtered oxide and nano-composites thin films and the study of their microstructure as well as their electrical, magnetic and optical properties. He developed sputtered ferrite thin films to be integrated as sensitive layers in magneto-optical disks and micro-bolometers (IR sensors). His work is currently focused on transparent conducting oxides, thermoelectric oxide layers and semiconductor sensitive layers for gas sensors.

Gemma Garcia Mandayo (PhD, female) is a Researcher and Project Manager in the Information and Communications Technology Division of Ceit-IK4 (Research Institute in San Sebastian, Spain) and Professor and Director of the Master in Telecommunication Engineering at Tecnun, Engineering School of the University of Navarra. She obtained her Degree in Electronics Engineering (1996) and her Doctorate (2002) from the University of Navarra. Her main research and technical interests are in the field of micro and nanosystem technology applied to sensing devices for industrial and environmental applications, focusing on the development of innovative sensor solutions. She has participated in 32 national and international research projects, 9 of them as main researcher and 5 as coordinator, with mainly an applied research scope. She has supervised three doctoral theses and is author or co-author of 25 scientific contributions in peer-reviewed journals and more than 50 international conferences of relevance in the Microelectronics and Sensors fields (7 invited conferences and 21 oral contributions). She is an active referee of the scientific publishing houses Elsevier, Wiley and MDPI Online and evaluator of scientific projects for public agencies such as ANEP in Spain and the European Commission.

WO_3 processed by direct laser interference patterning for NO_2 detection

L. Parellada-Monreal[a,b,*], S. Gherardi[c], G. Zonta[c,d], C. Malagù[c,d], D. Casotti[d,e], G. Cruciani[d], V. Guidi[d,e], M. Martínez-Calderón[a,b], I. Castro-Hurtado[a,b], D. Gamarra[f], J. Lozano[f], L. Presmanes[g], G. G. Mandayo[a,b]

[a] *1Ceit, Manuel Lardizabal 15, 20018 Donostia / San Sebastián, Spain.*
[b] *Universidad de Navarra, Tecnun, Manuel Lardizabal 13, 20018 Donostia / San Sebastián, Spain*
[c] *SCENT, S.r.l., Ferrara, Italy*
[d] *Department of Physics and Earth Science, University of Ferrara, Via Saragat 1/c, 44122 Ferrara, Italy*
[e] *INFN section of Ferrara, Via Saragat 1/c, 44122 Ferrara, Italy*
[f] *Escuela de Ingenierías Industriales, University of Extremadura, Badajoz, Spain*
[g] *Institut Carnot CIRIMAT, UPS-INPT-CNRS 5085, University Paul Sabatier, Toulouse, France*

Abstract

In this paper two kind of sensors based on WO_3 sputtered by magnetron sputtering and annealed at 600 °C have been studied. The first kind was processed by two-dimensional direct laser interfering patterning (DLIP) and the second one without any additional treatment. Morphological and structural characterization have shown a hole structure in a periodic line-pattern for the DLIP-processed sensors and a flat surface for the only-annealed sensors, both with a tetragonal WO_3 phase. TOF-SIMS analysis has revealed that the first WO_3 layers are reduced for both samples, which could improve sensing performance. Promising response enhancement of DLIP-processed sensors has been observed for low concentrations of NO_2 (from 0.5 ppm to 5 ppm) at 200 °C, lowering the limit of detection (LOD) to 10 ppb, half of the LOD of the only-annealed sensors (20 ppb). Cross sensitivity to CO and HCHO have been investigated and the sensing mechanisms discussed.

*Corresponding author
Email address: lparellada@ceit.es (L. Parellada-Monreal)

Keywords: WO_3, DLIP, tetragonal phase, TOF-SIMS, NO_2, Arrhenius

1. Introduction

In the recent years, special attention has been paid to nanostructured materials for gas sensors, since they open a window of distinctive physical properties for a wide range of materials [1] and the physics behind is based on surface reactions [2, 3]. The first chemical sensor based on nanobelts was published in 2002 by the group of E. Comini [4], showing a new class of stable and very sensitive nanostructured materials for gas detection. The nanostructures preparation methods can tune their structural and morphological characteristics and this allows a controlled modification of the sensor properties and performances [5, 6, 7, 8].

Among the preparation methods, the direct laser interference patterning (DLIP) is a good candidate to modify the surface properties of metal oxide semiconductors, enhancing their sensitivity to specific gases. This technique presents some important advantages, since it combines laser heat with interference patterns able to nanostructure areas of about 1 cm^2 in less than a second. Moreover, the nanostructures can be patterned directly on the sensing device (in-situ), without the need to transfer them (ex-situ), as in the case of many bottom-up techniques.

DLIP was successfully applied to different typologies of materials like semiconductors [9], metals [10] and polymers [11], enhancing their properties for specific applications like doped ZnO for solar cells [12, 13], carbon films for tribological applications [14] and graphene oxide for humidity sensors [15].

Previous works show the good sensing capability of WO_3 towards NO_2 gas [16, 17], that is one of the most harmful air pollutants as it can cause eye irritation and severe respiratory complications [18, 19].

Outdoors NO_2 sources are mainly coming from automotive, chemical industry and it is also present in the acid rain, while home NO_2 sources are gas-fueled heating and gas-fueled stoves. Nowadays there is not a unanimous agreement

on the maximum acceptable levels of NO_2 gas exposure. Nevertheless, the Environmental Protection Agency (EPA) has set 53 parts per billion (ppb) as the highest allowable limit [20] and the World Health Organization (WHO) established that 0.1 ppm of NO_2 limit indoors [19].

Therefore, monitoring very low concentration of NO_2 is crucial to keep under observation its dangerous effects and reduce the impact on the environment and human beings.

In this work, both sensing devices, based on WO_3 thin films annealed at 600 °C and sensors annealed and processed with a two-beam DLIP set-up were fabricated and tested with gases. The structural properties of the thin films were characterized by surface and bulk techniques, in order to investigate the laser effect on the devices. Gas sensing performance was investigated for NO_2 detection. Conductance measurements as a function of temperature were performed in air and NO_2, in order to understand the sensing mechanism during detection process of NO_2.

2. Material and methods

2.1. Sensor fabrication

The WO_3 sensors were fabricated on 1 x 2 cm^2 polished alumina substrates (Fig. 1 (a)). First of all, a Pt heating resistance was deposited on the reverse side of the alumina substrate shaped by UV-photolithography and grown by DC sputtering in an Edwards ESM 100 system (Fig. 1 (b)). The lift-off process was carried out with acetone. The same fabrication steps were used to grow Pt interdigitated (IDT) electrodes for the electrical measurements (Fig. 1 (c)). The electrodes have a separation and width of 50 μm, a length of 0.9 mm and cover an area of 1 mm^2. In order to improve the adhesion of the metal to the substrate, a 25 nm-thick Cr layer was deposited under the 200 nm-thick sputtered Pt layer. Afterwards, 1 mm^2 WO_3 sensing layer was deposited on top of the Pt electrodes by photolithography followed by RF reactive magnetron sputtering with a metal oxide target of 99.99 % purity. The sputtering process

was performed in a Pfeiffer-Iontech system at 300 W of RF power in a mixed atmosphere of oxygen (40 %) and argon (60 %) and under $5{\cdot}10^3$ mbar of pressure. The sputtering time was 1 h, the deposition temperature was between 25 °C and 30 °C and as for the Pt, acetone was used for the lift-off process (Fig. 1 (d)). Finally, the sensor device was thermally stabilized in a quartz oven at 600° C during 4 hours in synthetic air (Fig. 1 (e)). The only-annealed samples were labelled TT600C. The annealing temperature was chosen considering previous results obtained by our research group [21].

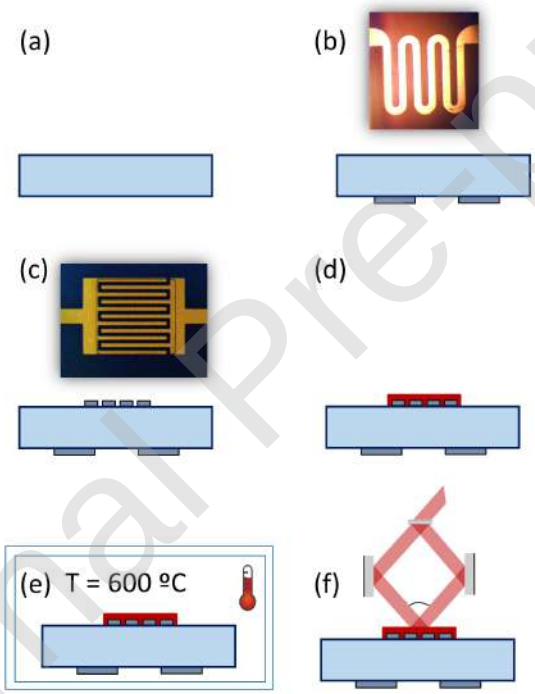

Figure 1: Scheme of the fabrication steps of the WO_3 sensor device. (a) Polished alumina substrate, (b) DC sputtering Pt heating resistance on the reverse side, (c) DC sputtering IDT electrodes, (d) RF sputtering of WO_3 sensing layer, (e) thermal annealing at 600 °C and (f) DLIP processing at 50 mJ/cm^2.

After annealing, some sensors were processed by two-beam DLIP set-up with a frequency tripled Q-switched Nd:YAG laser source provided by Thales, the Saga HP model (with a wavelength of 355 nm, a pulse duration of 8 ns,

a maximum energy of 600 mJ per pulse and a flat-top energy distribution) to obtain one-dimensional interference patterns on the surface (see Fig. 1 (f)). The interference patterns are a distribution of maximum and minimum intensity peaks, that lead to nanostructures down to a fraction of the laser wavelength.The areas of the material exposed to higher intensities than its ablation or annealing threshold are morphologically and structurally modified, getting melted or even removed, while areas exposed to lower intensities than these thresholds remain unaffected.

A detailed schematic drawing of the set-up is shown in Fig. 2: an optical beam splitter divides the laser source into two different beams; afterwards they are reflected in mirrors and finally addressed towards the sample surface with the same incident angle. The maximum and minimum of interference are indicated with a sinusoidal wave and the heat flux generated by the laser is indicated with red arrows. An example of a typical energy distribution of two-beam configuration DLIP is also shown. The maximum and minimum of interference are perpendicular to the IDT electrodes, as indicated by the coordinates in Fig. 2 (b).

The period of the structure (P, distance between two maxima or two minima of interference) is defined by the angle between the two laser beams (β) and the wavelength (λ):

$$P = \frac{\lambda}{2 \sin \frac{\beta}{2}} \tag{1}$$

In order to fabricate lines with a theoretical period of 500 nm, an angle of 41.5° was set-up. The necessary fluence to obtain one-dimensional interference patterns on the surface of WO_3 thin film annealed at 600 °C, was found to be optimum for a value of 50 mJ/cm^2 with a single shot. Samples processed at lower fluences than 50 mJ/cm^2 did not present any morphological modification. The DLIP-processed samples were labelled TT600C + DLIP50.

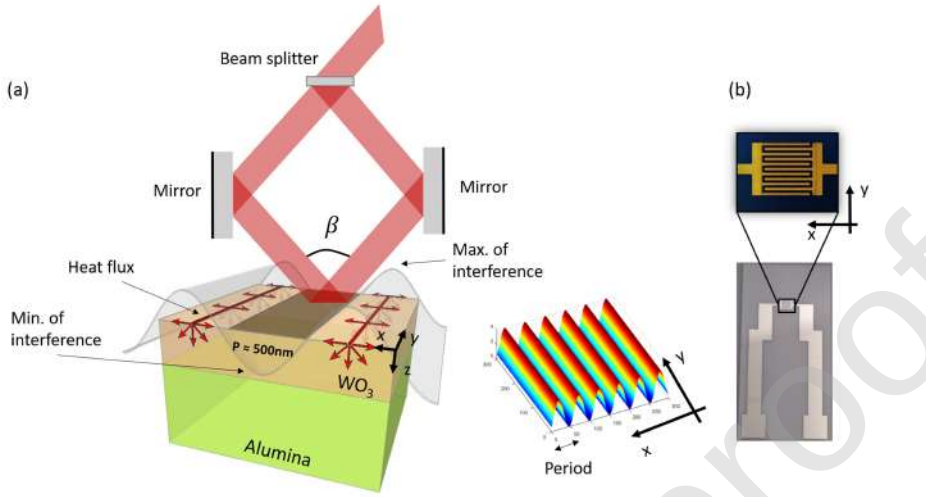

Figure 2: (a) Schematic two-beam DLIP set-up processing WO_3 thin film on alumina and an energy distribution simulation of one-dimensional pattern. (b) Detailed image of the IDT electrodes with the coordinates, indicating that the maximum and minimum of interference are perpendicular to the electrodes.

2.2. Film characterization

For the WO_3 film characterization, samples with a size of 6 x 7 mm^2 were fabricated by sputtering and annealed at 600° C following the same recipe as in previous section. Some samples have been also processed by DLIP, as explained in the sensor fabrication section.

The film thickness was determined by a KLA Tencor Profiler, resulting in an average thickness of 145 nm.

Regarding the morphological characterization, JPK Nanowizard 3 atomic force microscope (AFM) was employed. Tapping mode images were obtained using silicon Tap300-G cantilevers with a resonance frequency around 300 kHz. The tip radius is smaller than 10 nm and the half-cone angle is around 25 °.

A scanning electron microscopy (SEM) Quanta 3D FEG from FEI Company was used to study the homogeneity of the DLIP process in the sample as well as for a cross-section analysis.

The X-ray diffraction analysis was performed by a Bruker D8 Advance

diffractometer in grazing incident (GIXRD) configuration (1.8 ° incident angle). The diffractometer was equipped with a copper X-ray tube operating at 40 kV and 40 mA, and with a LYNXEYE XE detector. Samples were placed on a quartz zero-background holder. Measuring conditions were 5° to 80° 2θ-range, 0.02 2θ-scan rate, and 0.8 seconds per step of counting time. The mean crystallites size, the strain of the crystallites and the cell parameters were determined by whole profile fitting Powley and Le Bail methods [22, 23] as implemented in the TOPAS v 4 program by Bruker AXS [24]. The fundamental parameters approach was used for the line-profile fitting [25, 26, 27]. In this approach, the instrumental component of peak broadening is calculated by the convolution of instrument profile functions for optics and X-ray tube emission. Thus, the sample components to peak broadening (crystallite size and strain) are the only peak shape parameters to be optimized in the profile fitting procedure. In particular, the Double-Voigt method [28] implemented in TOPAS allowed to calculate the crystallite size and strain as volume-weighted for the mean column heights based on the sample-dependent integral breadths of peaks.

Raman spectra were collected under ambient conditions using Horiba Jobin Yvon LabRAM HR 800 spectrometer equipped with a fiber coupled 532 nm laser. Spectra acquisition was carried out using a x100 objective lens and 1800 gr/mm grating. During the measurement, the resulting laser power at the surface of the sample was adjusted to 4 mW. Exposure time ranged from 100 to 200 seconds.

The composition depth profile of different ions was measured using a time of flight secondary ion mass spectrometer (TOFSIMS 5, ION TOF). The mass spectrum was obtained by measuring the time-of-flight distribution of the positive ions coming from the sample surface into the detector. The primary ions source was Bi^+ operating at 25 keV and the spot size for the depth profile was 50 μm x 50 μm. Sputtering was done using 1 keV oxygen beam over a 300 μm x 300 μm of raster size area.

2.3. Electrical characterization

The response of the sensors was carried out by flowing the gases, controlled by mass flow controllers (MFC), into two cylindrical aluminium chambers of 600 and 10.8 ml.

The larger chamber was used to test the sensors at different temperatures (150 - 400 °C) for 5 ppm of NO_2. At the optimal temperature, lower NO_2 concentrations were tested, as well as NO_2 mixtures with CO and HCHO. The total flux into the chamber was set at 500 sccm and the uniformly gas distribution was guaranteed by a diffuser placed at the bottom of the chamber with holes disseminate at its surface.

The small chamber was used to perform the Arrhenius plots, following the steps below reported:

(i) In 400 sccm of air, the sensor was heated to 450 °C in less than 30 minutes and left for 10 minutes.

(ii) The sensor was cooled down to $\sim$ 100 °C and after a minute, the temperature was increased up to $\sim$ 500 °C with steps of $\sim$ 5 °C/minute.

(iii) The same procedure was performed in 5 ppm of NO_2.

The NO_2, CO and HCHO gases were taken from certified bottles mixed with synthetic air (Air Liquide).

The circuit used to measure the sensors conductance in the presence of gas includes an inverting operational amplifier (OA) (see Fig. S1 in the Supporting Information). R_s and R_f are the sensor and the reference resistance, respectively. R_f can be freely modified and must be in the same order of magnitude as R_s. As V_{in} and R_f are known and constant, the output voltage, V_{out}, is proportional to the conductance of the sensor, G, as indicated in equation 2:

$$V_{out} = -\frac{R_f}{R_s} \cdot V_{in} = const. \cdot G \tag{2}$$

The output voltage is measured through a Keithley 2000 Multimeter connected via GPIB to the computer, where a Labview© is acquiring the data.

The power consumption of the Pt heating element was doubly calibrated with a thermographic camera and a Pt100 resistance, so the heater is power controlled by a voltage source. Information regarding the calibration is introduced in the Supporting Information.

In this work, the response of the devices, SR, is defined as equation 3:

$$SR = G_{air}/G_{gas} \tag{3}$$

where G_{air} is the conductance of the sensor in air (baseline), and G_{gas} represents the sensor conductance after 30 minutes of gas exposure. The recovery time is defined as the time elapsed until the 10% of the initial baseline resistance is reached after the gas extraction.

3. Characterization results

3.1. Morphological and structural characterization

The AFM image of Fig. 3 (a) shows a flat surface for the sample thermal annealed WO_3 at 600 °C with a root-mean-square (RMS) roughness of 7 nm, while for the DLIP-processed sample (Fig. 3 (b) and (d)) a hole structure appears in a periodic line-pattern. The RMS roughness, as the average between the processed and non-processed regions, has increased to values between 10 and 15 nm. The profile section of the DLIP-processed sample measured from the AFM images (Fig. 3 (c)) indicates that the average depth of the holes is 18 nm. Nevertheless, from the cross-section images performed by FIB (Fig. 4), the hole structure seems to be reaching the substrate, so probably the profile sections of Fig. 3 (c) are underestimating the depth due to the high half-cone angle of the tip.

The line-patterned morphology indicates that the hole area corresponds to the places where higher intensity has been accumulated and consequently a higher temperature has been reached, melting material. Precisely, the highest area around the holes (Fig. 3 (d)) seems to be the melted WO_3 moved from inside the cavities, as explained by the Marangoni convection mechanism [29].

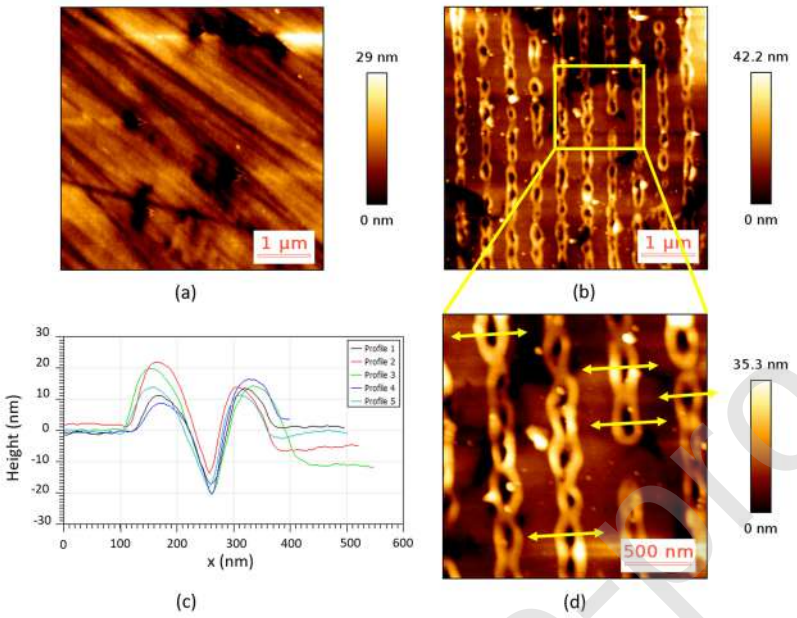

Figure 3: AFM tapping mode images of WO_3 thin film (a) only-annealed and (b) DLIP-processed. (c) Profiles of the sections point out in (d); (d) zoomed image of the sample DLIP-processed.

From the SEM images (see S1 in the supporting information), a bigger area of the nanostructured sample can be analysed, showing a great homogeneity of the nanostructuring with the desired period.

Many polymorphic structures have been identified in WO_3 as a function of temperature [30, 31, 32, 33, 34]: monoclinic (for temperatures lower than -50 °C and from 17 °C to 330 °C), triclinic (from -50 °C to 17 °C), orthorhombic (from 330 °C to 740 °C) and tetragonal (for temperatures higher than 740 °C). Not all the transitions are reversible and the lattice constants of each crystal structure can be found in [35]. The sensing performance is expected to be affected by the crystal structure as shown by I. M. Szilàgyi et. al., who found that monoclinic WO_3 shows good selectivity to H_2S, while hexagonal WO_3 sensors present lower sensitivity but much faster response [36].

The GIXRD patterns of the as-grown, only-annealed (TT600C) and DLIP-

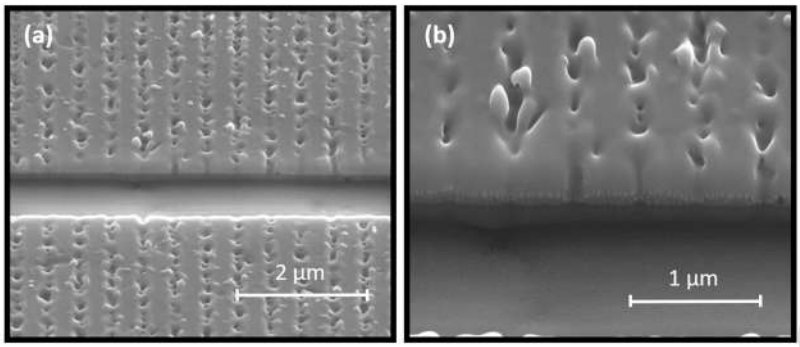

Figure 4: (a) SEM image of a cross-section of the sample DLIP-processed and (b) a zoom SEM image of (a).

processed (TT600C + DLIP50) samples are reported in Fig. 5. All patterns show peaks corresponding to the alumina substrate (space group $R\bar{3}c$, PDF 010-0173). The as-grown sample does not show peaks attributable to any WO_3 crystalline structure, while the only-annealed and DLIP-processed samples show peaks belonging to the tetragonal WO_3 structure (space group P4/nmm, PDF 018-1417), but the relative intensity of the (110) peak does not match the PDF data for powder tetragonal WO_3 structure, indicating that in both samples the crystallites grow with significant preferential orientation. This result is in agreement with previous investigations [21] and indicates that the laser modifications does not destabilize the tetragonal crystal structure. The stability of the crystal structure and the crystal size are important issues for the sensing mechanism [37].

Table 1 reports the cell parameters, the mean crystallites size and microstrain of the crystalline samples. Cell parameters and strain, that were calculated by Powley and Le Bail methods, are also very similar for both the samples treated and not treated with laser. Nevertheless, even if it remains within the error bars, a slight increase of the crystallite size of the DLIP-processed sample compared to only-annealed WO_3 has been observed.

Tetragonal phase of WO_3 is expected to appear for temperatures higher than 740 °C in bulk WO_3 [34] and the annealing performed in this work is at

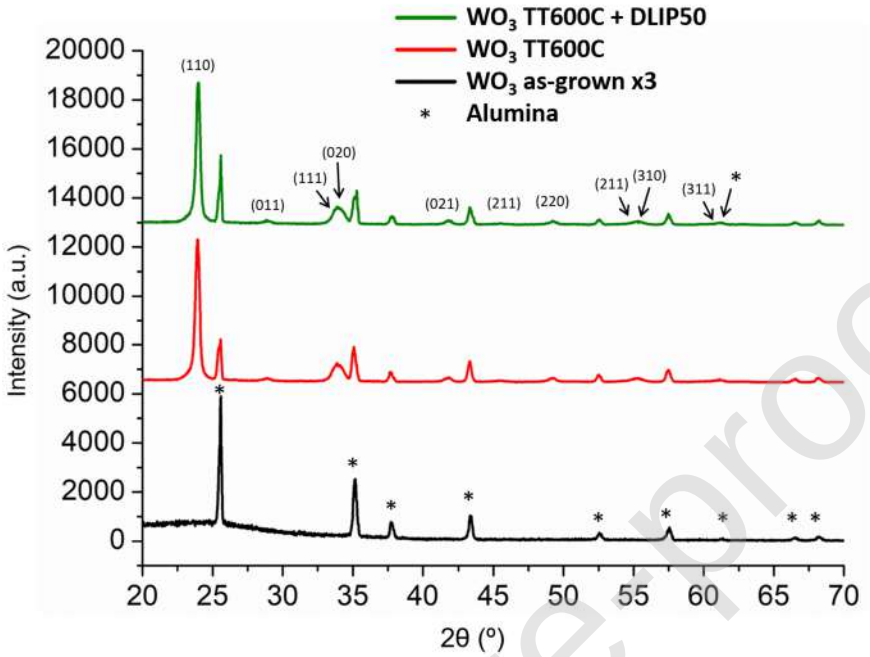

Figure 5: GIXRD measurements of the WO_3 thin film as-grown, WO_3 only-annealed and WO_3 DLIP-processed. All patterns show peaks of the Al_2O_3 substrates marked with $*$, the other peaks are attributable to WO_3 tetragonal phase.

600 °C. Nevertheless, in structures with nanometric crystals, as it is the case of the samples here, temperature and pressure of phase transitions can be strongly modified. A downshift in temperature for the tetragonal transition is shown in [38] for crystal sizes between 16 and 60 nm and the samples analysed here are in this range, as shown in Table 1.

Raman spectra (see Fig. 6) supports the above considerations. The as-grown samples only show peaks coming from the alumina substrate [39] (highlighted with an asterisk in Fig. 6) while both samples types (only-annealed and DLIP-processed) present the same WO_3 Raman modes for the measured spectra.

The peaks coming from the WO_3 thin film are found at 267.7, 692.1 and 802.4 cm^{-1}. As it is known, the peaks at low frequencies (200 - 500 cm^{-1}) correspond to bending vibrations, while the high frequency-ones that appear at

Table 1: Cell parameters, mean crystallite size and microstrain calculated by Le Bail and Powley methods for the two different samples.

Method	**Parameters**	**WO_3 TT600C**	**WO_3 TT600C + DLIP50**
Le Bail	a (Å)	5.2288(2)	5.2288(2)
	c (Å)	3.7963(6)	3.7974(8)
	size (nm)	47(3)	51(5)
	strain	0.24(1)	0.24(1)
Powley	a (Å)	5.2286(2)	5.2287(3)
	c (Å)	3.7955(7)	3.7967(9)
	size (nm)	44(3)	49(6)
	strain	0.23(1)	0.23(2)

frequencies between 600 and 1000 cm^{-1} are stretching modes [40]. Therefore, the lowest peak can be associated to a bending mode δ(O-W-O) [41] and the peaks in the range of 700 to 800 cm^{-1} are related to stretching modes O-W-O [42] and W^{6+}-O [41], respectively.

3.2. TOF-SIMS characterization

Positive TOF-SIMS in-depth experiments were performed to analyse the qualitative composition of the samples as a function of thickness. The detected ions related to WO_3 were W^+, WO^+ and WO_2^+ and the alumina related ions detected were Al^+ and AlO^+.

The measurements were performed twice at different sample areas with high repeatability of the results. In Fig. 7, only AlO^+ (for alumina) and W^+, WO^+ and WO_2^+ ions (for WO_3) of one of the measurements have been plotted, representing the sample behaviour. The signals shown in Fig. 7 have been filtered in order to reduce the noise generated by the equipment. The steepy increase

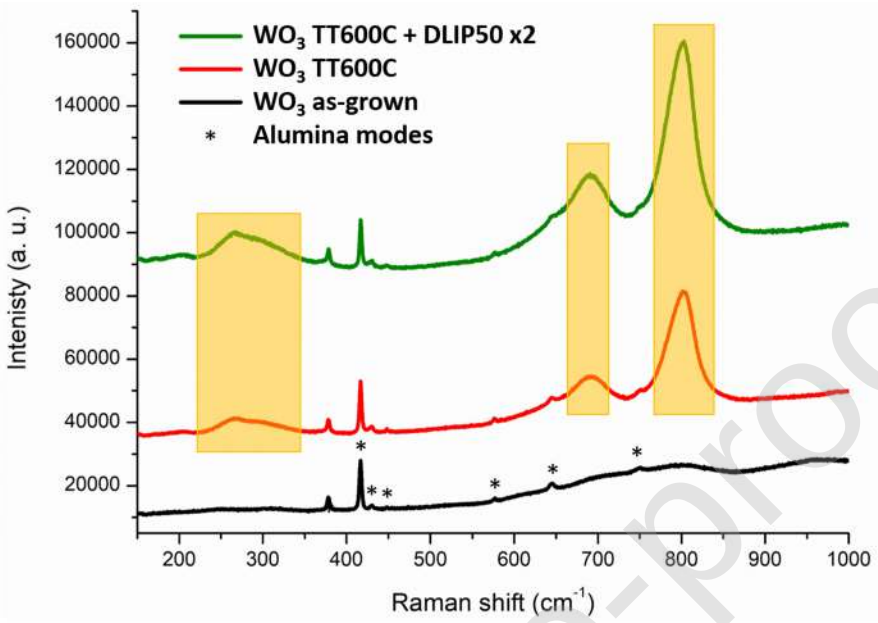

Figure 6: Raman spectra of the WO_3 thin film as-grown, WO_3 only-annealed and WO_3 DLIP-processed.

in the intensity for the ion WO_2^+ in the as-grown sample and the slow decrease of W^+ indicate that the sample is getting more oxidized as a function of the WO_3 sample depth. By contrast, in the other two samples, only a slight increase of the WO_2^+ and a decrease of W^+ before stabilization is shown. This result means that the first layers of the WO_3 are reduced, compared to the rest of the thin film and this could be explained by the existence of oxygen vacancies. As it is known, surface defects promote the gas detection and specially oxygen vacancies have been widely investigated as they increase the adsorption of gas molecules [43, 44, 7, 45, 46]. Moreover, the intensities of WO^+ and WO_2^+ ions are more parallel for the WO_3 DLIP-processed thin film, compared to only-annealed one (see Fig. 7 (b) and (c)). This can be originated by a higher homogeneity degree.

The sputter rate during the TOF-SIMS measurements has been calculated taking into account the WO_3 thickness deduced from cross-sections observed by

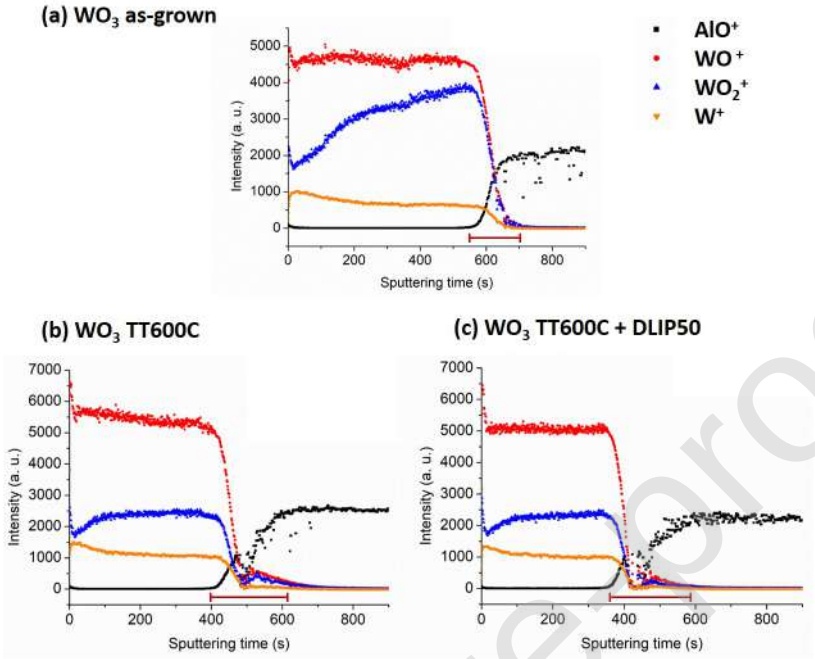

Figure 7: TOF-SIMS measurements of AlO^+, WO^+ and WO_2^+ ions for the samples (a) WO_3 as-grown, (b) WO_3 only-annealed and (c) WO_3 DLIP-processed.

SEM. A small increase of the sputter rate is observed comparing the as-grown with the only-annealed and DLIP-processed sample (see Table 2). This could be due to the increase of the homogeneity of the laser-treated sample that raises the sputter velocity. The interface region between the thin film and the WO_3 is also shown in Table 2 and indicated in garnet in Fig. 7. As it is expected, the interface region increases significantly with the annealing (62.9 nm) compared to as-grown (39.8 nm), because the atoms receive more energy. Therefore, a slight inter-diffusion can occur at the interface between the WO_3 layer and the alumina substrate. In the case of the sample also treated by DLIP, even a larger interface region (75.2 nm) is shown. This is explained by the higher temperatures (around 1000 K) that the sample reaches with the laser shot, although the shot time is in the nanosecond scale. Similar results were found for ZnO processed by DLIP at different fluences [9].

Table 2: Sputter rate during the TOF-SIMS measurements and interface region between the alumina and the thin film of the WO_3 as-grown, WO_3 only-annealed and WO_3 DLIP-processed.

Sample	Sputter rate (nm/s)	Interface region (nm)
As-grown	0.22	39.8
WO_3 TT600C	0.27	62.9
WO_3 TT600C + DLIP50	0.32	75.2

It is well known that the diffusivity has a great role on the sensitivity and the response time as demonstrated by G. Sakai et al. [47]. The surface patterned by DLIP has clearly a higher surface to volume ratio due to the holes generated in the thin film that should improve the gas diffusion. However it remains difficult to measure such surface enhancement factor since the size of the samples is much too small to be able to carry out surface measurements by gas adsorption [48].

4. Sensor results and discussion

Due to the importance of the working temperature during the gas detection, the response to 5 ppm of NO_2 at different stationary temperatures (150 °C - 400 °C) is reported in Fig. 8. Two sensors of each type are plotted, showing a good reproducibility between sensors of the same type. At temperatures $\geq$ 250 °C, DLIP-processed sensors respond to NO_2 by decreasing their conductivity but with a very low response, between 1.18 and 1.58. By contrast, sensors only-annealed at 600 °C do not detect NO_2 for these temperatures or increase their conductivity (although the conductivity is increasing, the response is calculated through equation (3) because NO_2 is an oxidizing gas). The values of the response for only-annealed sensors at temperatures $\geq$ 250 °C range from 1.03 to 0.55.

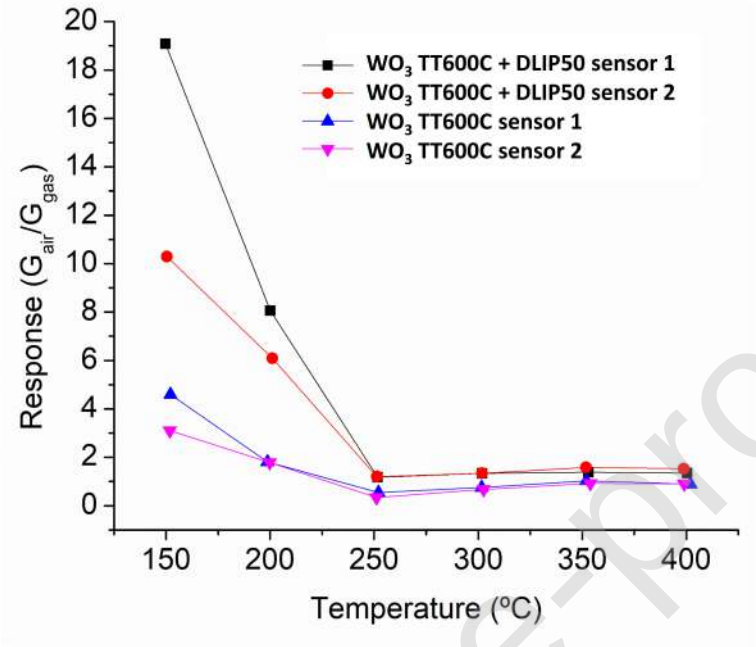

Figure 8: Response as a function of temperature for 5 ppm of NO_2 for two sensors DLIP-processed and two sensors only-annealed.

For temperatures lower than 250 °C, the response of both sensors increases while decreasing the temperature, but DLIP-processed sensors present responses $\simeq 3.5$ times higher than only-annealed sensors. Due to the long recovery time at 150 °C (48 minutes for only-annealed sensors and 13 minutes for DLIP-processed sensors), the chosen optimal temperature was 200 °C for both sensors, where the recovery times were decreased to 10 and 7 minutes, respectively.

The sensitivity of the sensors at the optimal temperature was studied by the response obtained at different NO_2 concentrations (Fig. 9 (a)). From the sensitivity graph (see Fig. 9 (b)), two different slopes can be observed for concentrations higher and lower than 2 ppm. The average sensitivity values obtained for higher concentrations are 1.74 and 0.47 ppm^{-1} for DLIP + TT600C and TT600C, respectively. Nevertheless, for the lower ones, the sensitivity values of both sensor type decrease to 0.95 and 0.20 ppm^{-1} for DLIP + TT600C and

TT600C, respectively, but the reproducibility of the sensors is higher.

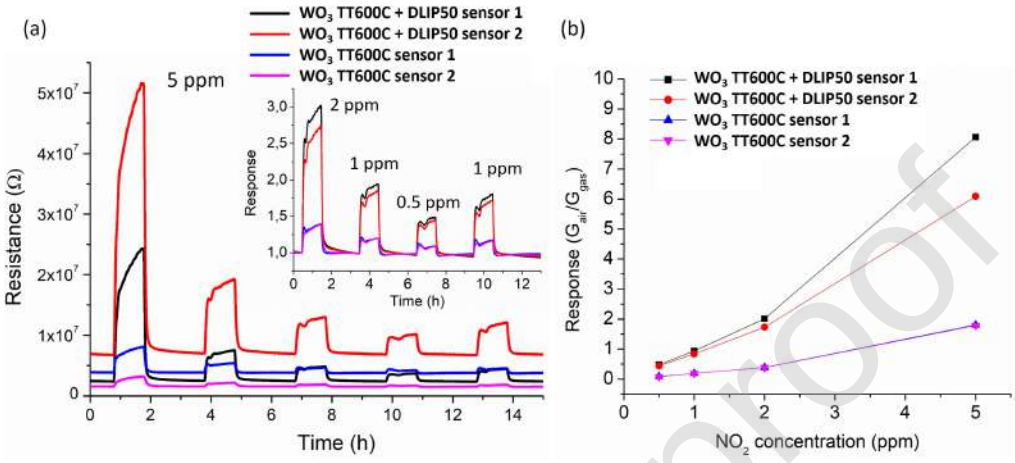

Figure 9: (a) Resistance variation of two sensors DLIP-processed and two sensors only-annealed for 5, 2, 1, 0.5 and 1 ppm of NO_2 at 200 °C. Response of the low concentrations are shown as an inset. (b) Sensitivity of the different sensors at 200 °C for concentrations between 0.5 and 5 ppm of NO_2.

The limit of detection (LOD) has been calculated using the following approximation, as reported in [49]: LOD = 3σ/b, where σ is the standard deviation of the baseline during 5 min and b is the slope of the sensitivity curve in the concentration range of 0.5 ppm - 2 ppm. Nevertheless, in order to give an exact value of the LOD, measurements with ppb levels of NO_2, such as the reported in [50] should be performed. The results show that in the sensors processed by laser (LOD = 10 ppb), the LOD decreased to half of the value of only-annealed samples (LOD = 20 ppb).

In order to study the cross sensitivity, mixtures of some interfering gases with 5 ppm of NO_2 have also been tested at 200 °C, as shown in Fig. 10 (the error bars of the final resistance values have been calculated with the data of two different sensors). Common concentrations of interest for the interfering gases have been chosen: 25 ppm of CO and 5 ppm of HCHO. The results show that the NO_2 oxidizing contribution is dominant, overcoming the reducing interference, especially for the DLIP-processed sensors. The performance of DLIP-processed

sensors makes them suitable to be employed as NO_2 sensors in atmospheres with CO and HCHO.

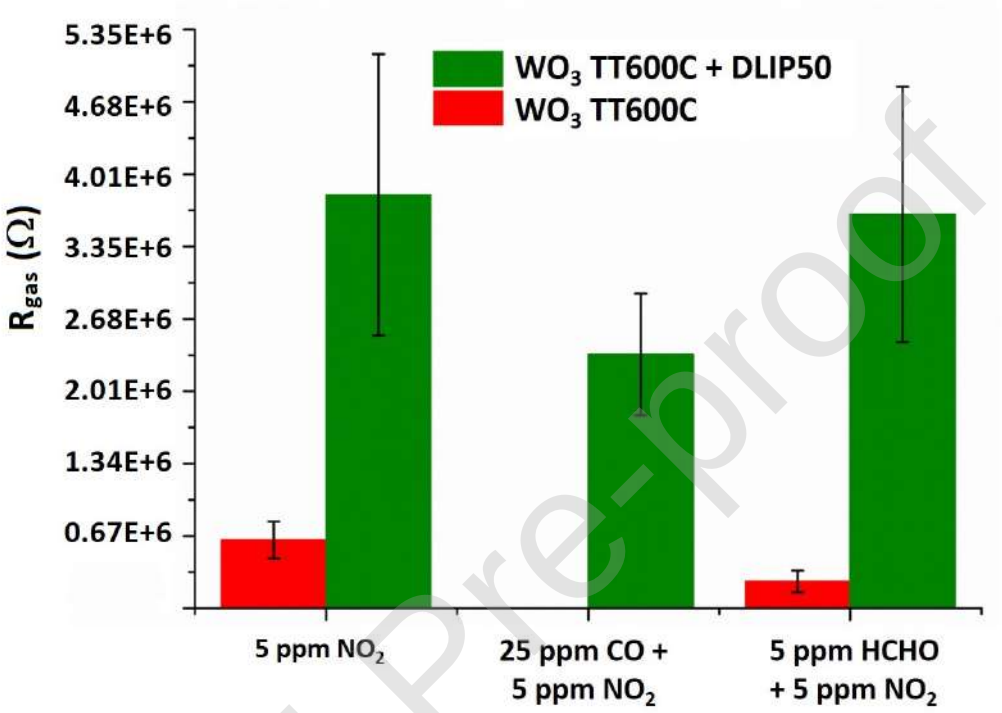

Figure 10: Responses at 200 °C for 5 ppm of NO_2, 5 ppm of HCHO + 5 ppm of NO_2 and 25 ppm of CO + 5 ppm of NO_2.

As shown in the previous section, significantly different responses have been found for the two type of sensors tested in the experimental conditions considered in the present work. Therefore, different detection mechanisms can be suggested in the two cases.

For low temperatures (T < 250 °C) it is generally accepted that reaction (4) takes place, where NO_2 reacts directly with the semiconductor surface, generating adsorbed NO_2 species and, consequently, decreasing the conductivity of the material [51, 52, 53].

$$NO_{2(g)} + e^- \Longrightarrow NO^-_{2(ads)} \tag{4}$$

At higher temperatures, the reducing behaviour of NO_2 has also been reported for WO_3 based sensors [54], as in the current case for the only-annealed sensors. It is accepted that NO_2 gas is adsorbed on the WO_3 surface forming nitrito type adsorbates (ONO^-) that after dissociate into nitrosyl type adsorbates (NO^-, NO^+). The reducing response observed for temperatures above 250 °C might be due to superior number of NO^+ adsorbates than NO^- [54].

According to the work of N. Yamazoe et al. [55], in the case of oxidizing gases and especially for NO_2 it had been demonstrated that a shielding effect can occur due to the oxygen contained in the background gas. In this case the power law is no more effective for very low NO_2 concentrations. The determination of the LOD by extrapolating the sensitivity curve to very low NO_2 concentration could therefore be not accurate and it would be better to make the measurements at low concentrations.

At 200 °C, the main difference between the detection mechanism of reducing and oxidizing gases is that while reducing gases interact with the adsorbed oxygen species, oxidizing agents such as NO_2 tend to be directly adsorbed on the surface (reaction 4). On WO_3 material is difficult to absorb oxygen in an active form such as O^- and consequently the reducing agents (CO and HCHO) do not strongly modify the NO_2 response, leading to good selectivity to the oxidizing gas, specially for DLIP-processed sensors.

In order to understand the oxygen species adsorbed in each type of sensor, the conductance has been measured as a function of the temperature as described in the experimental section. The Arrhenius plot in air and under 5 ppm of NO_2 are shown in Fig. 11. The method and analysis proposed by Lantto in [56] have been used to interpret the Arrhenius plot results obtained. This method relates the shape and slopes of the Arrhenius plots under different oxygen concentrations to the oxygen species adsorption. As it is also explained in [57, 58], the minimum in resistance (or maximum in conductivity) at low temperatures, in the conductance variation in air, is where the O^- adsorption starts counteracting the O_2^- adsorption,as can be seen in Fig. 11. The difference between conductivity curves in air and in air with 5 ppm of NO2 (looking

at the range from 150 °C to 250 °C) is bigger for the DLIP processed sensors, which may also be related to the fact that the DLIP processed sensors present higher response to NO_2. From Fig. 11, it can be appreciated that the slopes before and after the maximum in conductance for the DLIP-processed sensors are steeper than for only-annealed sensors, indicating that laser treated sensors present higher concentration of sites for adsorption or physisorption. This result highlights that the DLIP-processed sensors probably have laser-induced defects that work as adsorption sites, apart from the oxygen vacancies revealed by TOF-SIMS. This would enhance the NO_2 sensitivity, since more NO_2 molecules could be adsorbed, extracting electrons from the conduction band and thus increasing the resistance.

In fact, we consider that the conduction in tungsten oxide is mainly due to the oxygen vacancies with a contribution of the adsorbed oxygen, as shown by the different responses to oxidizing and reducing agents. In [59], the authors study the conductivity of sputtered and thermal evaporated WO3, whose morphology is similar to the reported in our study. In fact, the shape of the Arrhenius plot they present shows in similar experimental conditions shows correspondence to the reported in our study, with maxima and minima at similar temperatures.

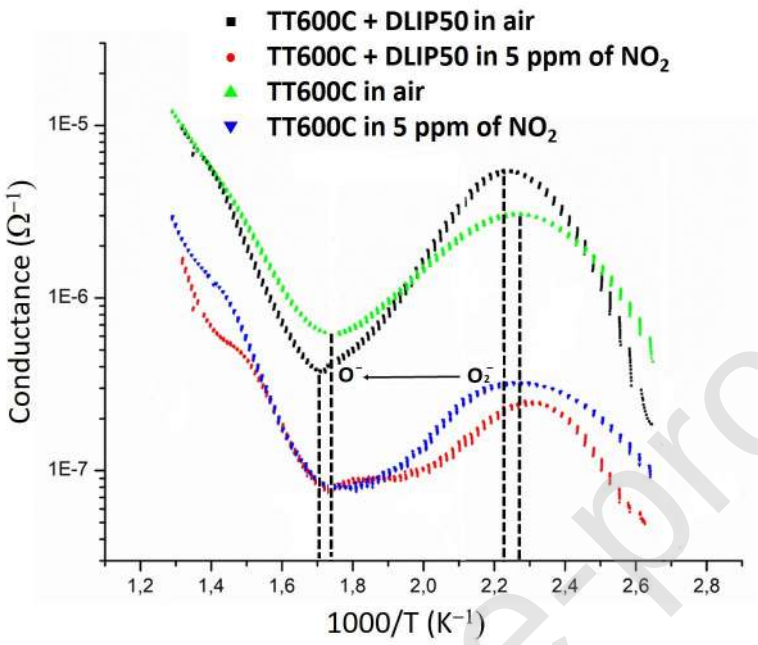

Figure 11: Arrhenius plots in air and in 5 ppm of NO_2 for the sensors only-annealed and DLIP-processed.

5. Conclusions

One-dimensional structures have been generated by DLIP technique on WO_3 thin film sensors after annealing and compared to only-annealed sensors. The surface morphology modification has not affected the crystal structure, which remains tetragonal for both films, with similar crystallite sizes. Raman characterization confirms the good crystalline structure of the WO_3 and TOF-SIMS analysis shows reduced layers on the top of the WO_3 film, probably due to oxygen vacancies.

Sputtered WO_3 based sensors processed by DLIP have shown responses $\simeq$ 3.5 times higher than only-annealed sensors to NO_2 at 200 °C. The LOD is 20 ppb for the only-annealed sensors and it decreases to 10 ppb for the DLIP-processed sensors. Besides, DLIP-processed sensors show low cross sensitivity to CO and HCHO, that makes them suitable for environmental applications.

Conductance variation as a function of temperature in air atmosphere and under 5 ppm of NO_2 points out that DLIP-processed sensors probably present a higher number of adsorption sites. This contributes to the enhancement of the NO_2 sensitivity.

References

[1] G. Jimenez-Cadena, J. Riu, F. X. Rius, Gas sensors based on nanostructured materials, Analyst 132 (11) (2007) 1083–1099.

[2] S. R. Morrison, Semiconductor gas sensors, Sensors and Actuators 2 (1981) 329–341.

[3] C. Wang, L. Yin, L. Zhang, D. Xiang, R. Gao, Metal oxide gas sensors: sensitivity and influencing factors, Sensors 10 (3) (2010) 2088–2106.

[4] E. Comini, G. Faglia, G. Sberveglieri, Z. Pan, Z. L. Wang, Stable and highly sensitive gas sensors based on semiconducting oxide nanobelts, Applied Physics Letters 81 (10) (2002) 1869–1871.

[5] Y.-F. Sun, S.-B. Liu, F.-L. Meng, J.-Y. Liu, Z. Jin, L.-T. Kong, J.-H. Liu, Metal oxide nanostructures and their gas sensing properties: a review, Sensors 12 (3) (2012) 2610–2631.

[6] L. Zhang, J. Zhao, J. Zheng, L. Li, Z. Zhu, Shuttle-like ZnO nano/microrods: Facile synthesis, optical characterization and high formaldehyde sensing properties, Applied Surface Science 258 (2) (2011) 711–718. doi:10.1016/j.apsusc.2011.07.116.

[7] M. Chen, Z. Wang, D. Han, F. Gu, G. Guo, Porous zno polygonal nanoflakes: synthesis, use in high-sensitivity no2 gas sensor, and proposed mechanism of gas sensing, The Journal of Physical Chemistry C 115 (26) (2011) 12763–12773.

[8] Z. Liu, M. Miyauchi, T. Yamazaki, Y. Shen, Facile synthesis and no2 gas sensing of tungsten oxide nanorods assembled microspheres, Sensors and Actuators B: Chemical 140 (2) (2009) 514–519.

[9] L. Parellada-Monreal, I. Castro-Hurtado, M. Martínez-Calderón, A. Rodriguez, S. Olaizola, D. Gamarra, J. Lozano, G. Mandayo, Study of sputtered zno modified by direct laser interference patterning: Structural

characterization and temperature simulation, Applied Surface Science 441 (2018) 331–340.

[10] M. Bieda, E. Beyer, A. F. Lasagni, Direct fabrication of hierarchical microstructures on metals by means of direct laser interference patterning, Journal of Engineering Materials and Technology 132 (3) (2010) 031015.

[11] A. F. Lasagni, D. F. Acevedo, C. A. Barbero, F. Mücklich, One-step production of organized surface architectures on polymeric materials by direct laser interference patterning, Advanced Engineering Materials 9 (1-2) (2007) 99–103.

[12] M. Soldera, K. Taretto, J. Berger, A. F. Lasagni, Potential of photocurrent improvement in μc-si: H solar cells with tco substrates structured by direct laser interference patterning, Advanced Engineering Materials 18 (9) (2016) 1674–1682.

[13] S. Ring, B. Stannowski, F. Fink, R. Schlatmann, Micro gratings written in zno: Al thin films using picosecond uv-laser interference patterning, physica status solidi (RRL)–Rapid Research Letters 7 (9) (2013) 635–638.

[14] T. Roch, V. Weihnacht, H.-J. Scheibe, A. Roch, A. F. Lasagni, Direct laser interference patterning of tetrahedral amorphous carbon films for tribological applications, Diamond and Related Materials 33 (2013) 20–26.

[15] L. Guo, H.-B. Jiang, R.-Q. Shao, Y.-L. Zhang, S.-Y. Xie, J.-N. Wang, X.-B. Li, F. Jiang, Q.-D. Chen, T. Zhang, H.-B. Sun, Two-beam-laser interference mediated reduction, patterning and nanostructuring of graphene oxide for the production of a flexible humidity sensing device, Carbon 50 (4) (2012) 1667–1673.

[16] X. Chen, Y. Shen, W. Zhang, J. Zhang, D. Wei, R. Lu, L. Zhu, H. Li, Y. Shen, In-situ growth of ZnO nanowire arrays on the sensing electrode via a facile hydrothermal route for high-performance NO_2 sensor, Applied Surface Science 435 (2018) 1096–1104.

[17] J.-S. Kim, J.-W. Yoon, Y. J. Hong, Y. C. Kang, F. Abdel-Hady, A. Wazzan, J.-H. Lee, Highly sensitive and selective detection of ppb-level NO_2 using multi-shelled WO_3 yolk–shell spheres, Sensors and Actuators B: Chemical 229 (2016) 561–569.

[18] L. S. Pilotto, R. M. Douglas, R. G. Attewell, S. R. Wilson, Respiratory effects associated with indoor nitrogen dioxide exposure in children., International Journal of Epidemiology 26 (4) (1997) 788–796.

[19] S. A. Abdul-Wahab, S. C. F. En, A. Elkamel, L. Ahmadi, K. Yetilmezsoy, A review of standards and guidelines set by international bodies for the parameters of indoor air quality, Atmospheric Pollution Research 6 (5) (2015) 751–767.

[20] J. M. Seguel, R. Merrill, D. Seguel, A. C. Campagna, Indoor air quality, American Journal of Lifestyle Medicine 11 (4) (2017) 284–295.

[21] I. Castro-Hurtado, T. Tavera, P. Yurrita, N. Pérez, A. Rodriguez, G. G. Mandayo, E. Castaño, Structural and optical properties of WO3 sputtered thin films nanostructured by laser interference lithography, Applied Surface Science 276 (2013) 229–235. doi:10.1016/j.apsusc.2013.03.072.

[22] G. Pawley, Unit-cell refinement from powder diffraction scans, Journal of Applied Crystallography 14 (6) (1981) 357–361.

[23] A. Le Bail, H. Duroy, J. Fourquet, Ab-initio structure determination of lisbwo6 by x-ray powder diffraction, Materials Research Bulletin 23 (3) (1988) 447–452.

[24] Bruker AXS GmbH. Karlsruhe, Germany, Bruker AXS. TOPAS 4-1, User Manual.

[25] R. W. Cheary, A. Coelho, A fundamental parameters approach to x-ray line-profile fitting, Journal of Applied Crystallography 25 (2) (1992) 109–121.

[26] R. W. Cheary, A. A. Coelho, J. P. Cline, Fundamental parameters line profile fitting in laboratory diffractometers, Journal of Research of the National Institute of Standards and Technology 109 (1) (2004) 1.

[27] E. J. Mittemeijer, P. Scardi, Diffraction analysis of the microstructure of materials, Vol. 68, Springer Science & Business Media, 2013.

[28] D. Balzar, Voigt-function model in diffraction line-broadening analysis, International union of crystallography monographs on crystallography 10 (1999) 94–126.

[29] J. Berger, T. Roch, S. Correia, J. Eberhardt, A. F. Lasagni, Controlling the optical performance of transparent conducting oxides using direct laser interference patterning, Thin Solid Films 612 (2016) 342–349.

[30] P. Woodward, A. Sleight, T. Vogt, Ferroelectric tungsten trioxide, Journal of Solid State Chemistry 131 (1) (1997) 9–17.

[31] R. Diehl, G. Brandt, E. Saije, The crystal structure of triclinic wo3, Acta Crystallographica Section B 34 (4) (1978) 1105–1111.

[32] T. Vogt, P. M. Woodward, B. A. Hunter, The high-temperature phases of wo3, Journal of Solid State Chemistry 144 (1) (1999) 209–215.

[33] E. Salje, The orthorhombic phase of wo3, Acta Crystallographica Section B 33 (2) (1977) 574–577.

[34] W. Kehl, R. Hay, D. Wahl, The structure of tetragonal tungsten trioxide, Journal of Applied Physics 23 (2) (1952) 212–215.

[35] H. Zheng, J. Z. Ou, M. S. Strano, R. B. Kaner, A. Mitchell, K. Kalantar-zadeh, Nanostructured tungsten oxide–properties, synthesis, and applications, Advanced Functional Materials 21 (12) (2011) 2175–2196.

[36] I. M. Szilágyi, S. Saukko, J. Mizsei, A. L. Tóth, J. Madarász, G. Pokol, Gas sensing selectivity of hexagonal and monoclinic wo3 to h2s, Solid State Sciences 12 (11) (2010) 1857–1860.

[37] G. Korotcenkov, The role of morphology and crystallographic structure of metal oxides in response of conductometric-type gas sensors, Materials Science and Engineering: R: Reports 61 (1-6) (2008) 1–39.

[38] M. Boulova, G. Lucazeau, Crystallite nanosize effect on the structural transitions of wo3 studied by raman spectroscopy, Journal of Solid State Chemistry 167 (2) (2002) 425–434.

[39] C. Bundesmann, N. Ashkenov, M. Schubert, D. Spemann, T. Butz, E. Kaidashev, M. Lorenz, M. Grundmann, Raman scattering in zno thin films doped with fe, sb, al, ga, and li, Applied Physics Letters 83 (10) (2003) 1974–1976.

[40] Y. Zou, Y. Zhang, D. Lou, H. Wang, L. Gu, Y. Dong, K. Dou, X. Song, H. Zeng, Structural and optical properties of wo3 films deposited by pulsed laser deposition, Journal of Alloys and Compounds 583 (2014) 465–470.

[41] V. Shapovalov, A. Komlev, V. VitâĂŹko, A. ZavâĂŹyalov, A. Lapshin, S. Moshkalev, V. Ermakov, Influence of annealing on the optical properties and chemical and phase compositions of tungsten-oxide films, Journal of Surface Investigation. X-ray, Synchrotron and Neutron Techniques 10 (5) (2016) 1077–1086.

[42] W. Wu, Q. Yu, J. Lian, J. Bao, Z. Liu, S.-S. Pei, Tetragonal tungsten oxide nanobelts synthesized by chemical vapor deposition, Journal of Crystal Growth 312 (21) (2010) 3147–3150.

[43] M.-W. Ahn, K.-S. Park, J.-H. Heo, J.-G. Park, D.-W. Kim, K. J. Choi, J.-H. Lee, S.-H. Hong, Gas sensing properties of defect-controlled zno-nanowire gas sensor, Applied physics letters 93 (26) (2008) 263103.

[44] W. An, X. Wu, X. C. Zeng, Adsorption of o2, h2, co, nh3, and no2 on zno nanotube: a density functional theory study, The Journal of Physical Chemistry C 112 (15) (2008) 5747–5755.

[45] M. Chen, Z. Wang, D. Han, F. Gu, G. Guo, High-sensitivity no2 gas sensors based on flower-like and tube-like zno nanomaterials, Sensors and Actuators B: Chemical 157 (2) (2011) 565–574.

[46] Y. Qin, Z. Ye, Dft study on interaction of no2 with the vacancy-defected wo3 nanowires for gas-sensing, Sensors and Actuators B: Chemical 222 (2016) 499–507.

[47] G. Sakai, N. Matsunaga, K. Shimanoe, N. Yamazoe, Theory of gas-diffusion controlled sensitivity for thin film semiconductor gas sensor, Sensors and Actuators B: Chemical 80 (2) (2001) 125–131.

[48] F. Oudrhiri-Hassani, L. Presmanes, A. Barnabe, P. Tailhades, Microstructure, porosity and roughness of rf sputtered oxide thin films: characterization and modelization, Applied Surface Science 254 (18) (2008) 5796–5802.

[49] J. Li, Y. Lu, Q. Ye, C. Martin, J. Han, M. Meyyappan, Carbon nanotube sensors for gas and organic vapor detection, Nano Letters 3 (7) (2003) 929–933.

[50] T. Kida, A. Nishiyama, Z. Hua, K. Suematsu, M. Yuasa, , K. Shimanoe, Wo3 nanolamella gas sensor: porosity control using sno2 nanoparticles for enhanced no2 sensing, Langmuir 30 (2014) 2571–2579.

[51] M. Epifani, J. D. Prades, E. Comini, E. Pellicer, M. Avella, P. Siciliano, G. Faglia, A. Cirera, R. Scotti, F. Morazzoni, et al., The role of surface oxygen vacancies in the no2 sensing properties of sno2 nanocrystals, The Journal of Physical Chemistry C 112 (49) (2008) 19540–19546.

[52] M. Hjiri, L. El Mir, S. G. Leonardi, N. Donato, G. Neri, Co and no2 selective monitoring by zno-based sensors, Nanomaterials 3 (3) (2013) 357–369.

[53] B. Xiao, D. Wang, F. Wang, Q. Zhao, C. Zhai, M. Zhang, Preparation of hierarchical wo3 dendrites and their applications in no2 sensing, Ceramics International 43 (11) (2017) 8183–8189.

[54] Y.-K. Chung, M.-H. Kim, W.-S. Um, H.-S. Lee, J.-K. Song, S.-C. Choi, K.-M. Yi, M.-J. Lee, K.-W. Chung, Gas sensing properties of wo3 thick film for no2 gas dependent on process condition, Sensors and Actuators B: Chemical 60 (1) (1999) 49–56.

[55] N. Yamazoe, K. Shimanoe, Theory of power laws for semiconductor gas sensors, Sensors and Actuators B: Chemical 128 (2) (2008) 566–573.

[56] P. Lantto V, Rompplainen, L. S, A study of the temperature dependence of the barrier energy in porous tin dioxide, Sensors and Actuatorsl 14 (2) (1998) 149–163.

[57] J. Samà, S. Barth, G. Domènech-Gil, J.-D. Prades, N. López, O. Casals, I. Gràcia, C. Cané, A. Romano-Rodríguez, Site-selectively grown sno2 nws networks on micromembranes for efficient ammonia sensing in humid conditions, Sensors and Actuators B: Chemical 232 (2016) 402–409.

[58] S.-C. Chang, Oxygen chemisorption on tin oxide: correlation between electrical conductivity and epr measurements, Journal of Vacuum Science and Technology 17 (1) (1980) 366–369.

[59] M. Gillet, C. Lemire, E. Gillet, A. K, The role of surface oxygen vacancies upon wo3 conductivity, Surface Science 532-535 (2) (2003) 519–525.

- WO_3 sensors only-annealed and processed by DLIP after annealing have been fabricated
- Two-dimensional DLIP generates stripes with a hole structure on the WO_3 surface
- Tetragonal crystal structure is shown for the two types of WO_3 layers
- DLIP processed sensing layers present great selectivity towards NO_2 with a LOD of 10 ppb
- NO_2 detection mechanism for the two types of sensors is discussed and analyzed